Deep structure of the lunar South Pole–Aitken basin

Peter B. James[1,2], David E. Smith[3], Paul K. Byrne[4], Jordan D. Kendall[5], H. Jay Melosh[6], Maria T. Zuber[3]

[1]Baylor University, Department of Geosciences, Waco, TX, USA.
[2]Lunar and Planetary Institute, Houston, TX, USA.
[3]Massachusetts Institute of Technology, Cambridge, MA, USA.
[4]North Carolina State University, Raleigh, NC, USA.
[5]NASA Goddard Space Flight Center, Greenbelt, MD, USA.
[6]Purdue University, West Lafayette, IN, USA.

Key Points:

- The southern interior of South Pole–Aitken (SPA) basin is underlain by anomalously dense mantle with more than 2×10^{18} kg of excess mass.
- A two-layered inversion of gravity and topography yields an average crustal thickness of at least 16 km in the basin interior.
- The free-air gravity anomaly is consistent with the presence of buried metal from the core of the basin-forming impactor in the lunar mantle.

This article has been accepted for publication and undergone full peer review but has not been through the copyediting, typesetting, pagination and proofreading process which may lead to differences between this version and the Version of Record. Please cite this article as doi: 10.1029/2019GL082252

Corresponding author: Peter James, `P_James@baylor.edu`

Abstract

The South Pole–Aitken (SPA) basin is a gigantic impact structure on the far side of the Moon, with an inner rim extending approximately 2000 kilometers in the long axis dimension. The structure and history of this basin are illuminated by gravity and topography data, which constrain the subsurface distribution of mass. These data point to the existence of a large excess of mass in the Moon's mantle under the SPA basin. This anomaly has a minimum mass of 2.18×10^{18} kg and likely extends to depths of more than 300 km. Plausible sources for this anomaly include metal from the core of a differentiated impactor or oxides from the last stage of magma ocean crystallization. Although the basin-forming impact event likely excavated the vast majority of the pre-existing crust, the present-day crust of the basin interior is at least 16 km thick in undisturbed regions.

1 Introduction

The South Pole–Aitken (SPA) basin is the largest preserved impact basin on the Moon and perhaps the largest universally recognized impact structure in the solar system. While larger impact events undoubtedly occurred throughout the solar system during planetary accretion, most indications of these events were erased through subsequent bombardment and thermally induced viscous relaxation. The SPA basin therefore is an important remnant of a process that shaped solar system bodies into their present forms. Moreover, the SPA basin is one of the oldest preserved structures on the Moon Evans et al. (2018); Hiesinger et al. (2012). Consequently, the formation and structure of the SPA basin hold important clues about the history and evolution of the Moon.

Recent geophysical datasets provide an opportunity to infer the structure of the crust and mantle under the SPA basin and to constrain its origin. The first such dataset is the lunar topography provided by the Lunar Orbiter Laser Altimeter (LOLA) onboard the Lunar Reconnaissance Orbiter (LRO) Smith et al. (2010), shown in Figure 1a. This instrument has collected nearly 7 billion topography measurements to date, and crucially, it has filled a polar gap in the Clementine data that were used by previous studies of SPA Garrick-Bethell and Zuber (2009). The Moon's topography is important for an inference of internal structure in two ways: it contributes to the gravity field observed above the Moon's surface, and its weight must be supported by stresses in the Moon's interior.

The second dataset enabling our analyses is the global gravity field recovered by NASA's Gravity Recovery And Interior Laboratory (GRAIL) mission Zuber, Smith, Lehman, et al. (2013); Zuber, Smith, Watkins, et al. (2013), shown in Figure 1b. Gravity datasets are commonly described in terms of spherical harmonic coefficients ?e.g.,¿[]wieczorek2015gravity. The resolution of the spherical harmonic expansion is related to the "degree" of the expansion, where higher degrees correspond to smaller spatial scales (i.e., wavelengths), and vice versa. Spherical harmonic coefficients for the gravity field have been determined up to degree 1200 (wavelength ∼9 km) by workers at NASA Goddard Space Flight Center Lemoine et al. (2014) and to degree 1500 (wavelength ∼7 km) by workers at NASA Jet Propulsion Laboratory Konopliv et al. (2014). In both solutions, the data signal exceeds the uncertainty by at least an order of magnitude for all spherical harmonic degrees less than 600. This precision is more than sufficient for any study of the crust–mantle interface or the underlying mantle.

2 Two-layered inversion of internal structure

GRAIL and LOLA data can reveal density anomalies in the Moon's upper mantle through a two-layered inversion of gravity and topography that minimizes residual stress in the lithosphere and residual Bouguer gravity Banerdt (1986); Herrick and Phillips (1992); James, Zuber, and Phillips (2013); James, Zuber, Phillips, and Solomon (2015). Such an inversion allows for elastic compensation of short-wavelength topography but obviates the need to invoke elastic compensation at the longest wavelengths. Note that this approach is not appropriate everywhere on the Moon; in particular, the lunar mascon basins and basaltic maria are clear examples of super-isostatic topography Melosh et al. (2013). However, the gravity data inside SPA are inconsistent with either of these phenomena: mascons and volcanic top-loading correspond to free-air gravity highs, while the SPA basin features a long-wavelength gravity low. In the absence of a plausible mechanism for the formation of long-wavelength, sub-isostatic topography, it is more reasonable to assume that residual stresses are in a minimized state.

In the inversion implemented here, topography is compensated by crust–mantle interface relief, by density variations in the crust inferred from iron abundance ?cf. Fig. S13 of¿[]wieczorek2012crust, and by dynamic flow stresses associated with lateral variations in mantle density, ρ_m. Mantle density is allowed to vary laterally throughout the upper mantle, from the crust–mantle interface down to a depth d_M. Beneath d_M we as-

Figure 1. (a) Orthographic projection of lunar topography as collected by the LOLA. The inner rim is outlined in black, and a central topographic depression is indicated with a white dashed circle. (b) Free-air gravity from GRAIL referenced to a radius of 1748 km, with the topographic depression from (a) marked.

sume that the mantle is homogeneous with a density equal to the average upper mantle density. Further specifics of the implementation are provided in the Supporting Information Hemingway and Matsuyama (2017); Hirth and Kohlstedt (2013); Matsuyama et al. (2016); Neumann et al. (2015); Sori et al. (2018); Wieczorek and Phillips (1998). The anomalous mantle mass per unit area for $d_M = 800$ km and an average mantle density of 3220 kg/m^3 is plotted in Figure 2.

Table 1. Best-fit ellipses for South Pole–Aitken basin

	Major axis	Minor axis	Tilt	Center coordinates
Inner Rim:				
Crustal thickness (36-km contour)	2015 km	1596 km	16.6°	(−55.4°N, 190.0°E)
LOLA topography (2-km contour)	1985 km	1488 km	17.5°	(−54.9°N, 189.5°E)
Clementine topography [a]	1940 km	1440 km	18.8°	(−53.2°N, 191.1°E)
Outer Rim:				
Clementine topography [a]	2402 km	2056 km	18.8°	(−55.0°N, 191.1°E)
Incomplete Exterior Scarp:				
LOLA-aided surface morphology	2701 km	2372 km	18° [b]	(−55°N, 190°E)[b]

[a] Garrick-Bethell and Zuber (2009)

[b] values assigned *a priori*

3 Best-fit ellipses for the basin margin

New geophysical data sets also provide new insights into the size and orientation of the South Pole–Aitken basin. While previous work by garrick2009elliptical used topography from the Clementine mission to demarcate the rims of SPA, those data had a gap southward of 70°S. The global coverage of topography from LOLA and gravity from GRAIL allows us to produce improved best-fit ellipses of the inner rim, as well as to produce comparable ellipses from crustal thickness. Our methodology is identical to that of garrick2009elliptical: we mapped landforms on the basis of having morphologies consistent with constituting the edge of the basin (e.g., isolated massifs) and with their coordinates solved for a best-fit ellipse in a stereographic projection. Best-fit ellipses for the −2 km topographic contour (mirroring the analysis of garrick2009elliptical) and the 36-km crustal thickness contour from "Model 3" of wieczorek2012crust are listed in Table 1 along with an exterior scarp associated with those massifs identified with LOLA topography.

Table 2. Total excess mass in the mantle under the SPA basin floor and the associated maximum density anomaly as a function of d_M, the depth of the lower extent of the mass anomaly beneath the mean radius of the Moon.

Depth of lower extent, d_M (km)	Total mass ($\times 10^{18}$kg)	Maximum density anomaly (kg/m^3)
200	4.20	27.4
400	2.69	14.1
600	2.36	11.7
800	2.30	10.5
1000	2.29	9.6
1200	2.26	9.0
Entire mantle	2.18	8.3

4 Discussion

4.1 Mass excess in the mantle

Our inversion reveals a conspicuous mass excess in the mantle under the SPA basin floor centered at approximately (200°E, 62°S) and spanning several hundred kilometers. The depth-distribution of this anomalous mass is not well constrained: it could be a large density anomaly distributed across a modest range of depths, or it could be a subtle density anomaly distributed throughout the depth of the mantle (Table 2). The total excess mass under the SPA basin is less dependent on model assumptions, though, with a peak anomaly of at least 6×10^6 kg/m^2 and an integrated total mass excess of at least 2.18×10^{18} kg, or approximately 0.003% of the Moon's total mass. The anomaly has no apparent correlation with surface mineralogy as detected by remote sensing D. P. Moriarty and Pieters (2018); Uemoto et al. (2017) or mare volcanism Wilhelms, John, and Trask (1987); see Fig. S5. The mass anomaly does coincide with the basin's central topographic depression (Fig. 1), previously interpreted to result from impact melt sheet contraction D. Moriarty and Pieters (2016); Ohtake et al. (2014). The depth of this depression is consistent with the 1–2 km downward deflection expected from the weight of the mantle mass anomaly **?**cf.¿[]richards1984geoid.

Figure 2. Mantle mass excess per unit area. A large excess of mass in the southern interior of the SPA basin coincides with the central depression outlined in Fig. 1 (outlined here with a dashed gray circle). Black lines mark the best-fit ellipses for the SPA basin's inner ring, outer ring, and exterior scarp we map, as specified in Table 1.

The origin of the observed mass excess under the SPA basin is constrained by plausible depth ranges, the geographic extent, and the magnitude of the mass anomaly. The required mass anomaly is smallest when it extends throughout the depth of the mantle (see Table 2). If confined to the uppermost 200 km of the Moon's interior, the inferred mass anomaly magnitude nearly doubles, and mantle anomalies with a lower extent of 100 km fail to converge (i.e., they cannot reproduce the observed gravity and normal stress data). Consequently, depths of at least 300 km for the lower extent of the mass anomaly are preferred. As such, impact melt pool cumulates lying tens of kilometers beneath the crust are unlikely to be the source of the observed mass anomaly. Thermally driven downwellings on the Moon are expected to occur at wavelengths larger than the observed anomaly Laneuville, Wieczorek, Breuer, and Tosi (2013); Roberts and Zhong (2006), so this phenomenon is unlikely to be responsible for the observed gravity signature. The titanium oxide-rich upper layers of the pre-overturn lunar mantle is expected to have had as much as $(1.2 \pm 0.2) \times 10^{21}$ kg more mass than the post-overturn mantle Elkins-Tanton, Burgess, and Yin (2011), so an inefficient mantle overturn that stranded oxides under SPA could sufficiently explain the magnitude of the observed mass anomaly. Another possible source of excess mass is the metal delivered by the impactor that formed the SPA basin. Hydrocode simulations of SPA formation predict that the core of a differentiated impactor would have been widely dispersed in the upper mantle Kendall and Melosh (2016), and the excess mass observed in the mantle is approximately equivalent to the mass excess that would result from dispersing a 95-km-diameter iron-nickel core (density contrast of 4800 kg/m^3) in the Moon's mantle.

The positioning of the mass anomaly under the SPA basin may also speak to its origin. If it corresponds to stranded oxides from magma ocean solidification, a mechanism for concentrating these oxides under the SPA basin should exist; we do not venture to propose any such mechanism here. If the mantle anomaly has an impact origin, the misalignment of the anomaly from the basin center ($\sim$400 km to the southeast) provides an important observational constraint for future basin formation simulations.

The existence of mantle mass anomaly in the present day—regardless of its origin—speaks to the rigidity of the lunar interior. If the emplacement of mass anomaly were contemporaneous with the basin-forming impact event 3.9–4.3 Gyrs before the present Evans et al. (2018); Garrick-Bethell and Miljković (2018); Wilhelms et al. (1987), the persistence of this mass anomaly places a lower bound on the viscosity of the deep mantle and an upper bound on its temperature. For example, a degree-10 harmonic load starting at depths of 50 km or greater would require a viscosity of at least 8×10^{21} Pa·s in the lower mantle to prevent the mass anomaly from sinking to near the core–mantle boundary (see the Supporting Information). Note that this constraint primarily corresponds to the mantle directly beneath SPA, which may be cooler than the mantle elsewhere on the Moon Laneuville, Taylor, and Wieczorek (2018). While this calculation does not incorporate time-varying viscosity, this constraint temporally corresponds to the latter half of lunar history when the sinking load is closest to the lower mantle and thus most sensitive to its viscosity. Nevertheless, these considerations make the viscosity constraint a conservative one. The translation of viscosity into temperature requires a knowledge of the mantle's rheology, which is poorly constrained, but diffusion creep of a dry lherzolite Hirth and Kohlstedt (2013) would yield an upper bound of 1480°C for the temperature of the lower mantle in the latter half of lunar history. Pockets of high-density material such as metal from an impactor core are capable of sinking to the Moon's core faster than a long-wavelength downwelling, but the sinking velocity inferred from Stokes'

Law is less than that of the long-wavelength downwelling for metal pockets smaller than 25 km in diameter. If the differentiated impactor core was largely dispersed into globules smaller than 25 km, it is plausible that some fraction of the impactor core remains suspended in the lunar mantle.

4.2 Crustal thickness in the basin interior

Nearly all of the crust pre-dating the SPA impact event was likely excavated during the basin-forming impact event along with a portion of the upper mantle Potter, Collins, Kiefer, McGovern, and Kring (2012). Consequently, any remaining crust must come from a combination of a few mechanisms, including inward flow of feldspathic crust immediately after the impact event Johnson et al. (2016), differentiation of an impact melt pool Hurwitz and Kring (2014); Vaughan and Head (2014), mare volcanism Pieters, Head, Gaddis, Jolliff, and Duke (2001), non-mare volcanism D. P. Moriarty and Pieters (2015), and late infill of ejecta Petro and Pieters (2004).

The crust inside the SPA basin is considerably more mafic than the Moon's feldspathic highland crust Jolliff, Gillis, Haskin, Korotev, and Wieczorek (2000), and the *a priori* choices of physical parameters such as crust–mantle density contrast influence the modelled thickness of the SPA's crust. Four crustal thickness models presented in wieczorek2012crust imply that crust in the center-most region of the SPA interior has a thickness of 13–22 km. When we use the same parameters as in the models of wieczorek2012crust, we generate crustal thickness maps that typically agree within ±2 kilometers for a given choice of parameters. This is illustrated in Figure 3 for "Model 1" of wieczorek2012crust, which is the model in that paper yielding the thinnest crust on the floor the SPA basin. One notable discrepancy occurs above the mantle mass excess described earlier, where our two-layered crustal thickness model infers a crust–mantle interface up to 3 kilometers deeper than that of the wieczorek2012crust models. This disagreement can be understood by the fact that all crustal thickness models minimize the residual Bouguer gravity anomaly at long wavelengths: a mass excess in the mantle would increase the Bouguer anomaly, and a deeper root of low-density crust reduces the Bouguer anomaly in kind.

Figure 3. Cross section of the SPA basin along the 200°E meridian with 10:1 vertical exaggeration. The interface between the crust and mantle is demarcated by a black line for the two-layered model. The comparable one-layered model of the crust–mantle interface (Model 1 of Wieczorek et al. (2013)) is plotted in red.

4.3 Orientation and excavation

The inner rim dimensions determined by mapping landforms identified with LOLA topography and GRAIL-derived crustal thickness largely agree with the previous analysis by garrick2009elliptical and a variety of mapped massifs described in the Supplementary Information Shoemaker, Robinson, and Eliason (1994); Speyerer, Robinson, Denevi, et al. (2011). In particular, the major axes of all ellipses have azimuths in a range of 16°–19° west of north or east of south. These orientations stand in contrast to the assumptions of previous work, notably schultz2011origin, which ostensibly required major axis azimuths of 50°–51°. Our analysis here finds an inner rim slightly larger than that of garrick2009elliptical thanks to new data near the south pole, and we identify an additional scarp exterior to the previously identified outer rim.

Crustal thickness models allow us to constrain the volumetric excavation of the crust associated with the impact event. If the pre-impact thickness is taken to be the mean crustal thickness at a distance of 2000 km from the basin center, an integration of crustal thickness within the SPA outer rim yields a crustal volume deficit of $(4.3-4.8)\times 10^7$ cubic kilometers for the models of wieczorek2012crust and a deficit of 4.1×10^7 cubic kilometers for the comparable two-layered model. If all of the crust within the inner rim were emplaced by subsequent processes such as melt sheet differentiation and ejecta from other basins, the volume of ejected crust rises to at least $9.4{\times}10^7$ cubic kilometers. The SPA impact may have also ejected significant volumes of the upper mantle, so these volumes represent conservative lower bounds on the total volume of ejecta.

5 Conclusions

We have found evidence for a large excess of mass in the Moon's mantle under the SPA basin. This anomaly has a minimum mass of $2{\times}10^{18}$ kg and likely extends to depths of at least 300 km. The presence of this mass anomaly implies that the central depression in the SPA basin floor is not caused by melt sheet contraction as was previously thought, but rather is weighed down by the excess mass in the mantle. The interior of the SPA basin contains a relatively uniform-thickness crust with the exception of superposed craters, with a thickness of at least 16 km in undisturbed regions. This is thicker than previous estimates, which magnifies the challenge of explaining the origin of the crust in the interior of the SPA basin.

There are at least two plausible explanations for the existence of a mantle mass anomaly: metal from the core of the basin-forming impactor that remains suspended in the Moon's mantle, or lingering oxide-rich dregs from the last stage of magma ocean crystallization. If the mass anomaly was emplaced contemporaneously with the formation of the basin, then the Moon's lower mantle has likely been cooler than approximately 1480°C in the latter half of lunar history. This is consistent with most seismically derived estimates of mantle temperature Gagnepain-Beyneix, Lognonné, Chenet, Lombardi, and Spohn (2006);

Khan, Connolly, Maclennan, and Mosegaard (2007) and implies that the Moon's interior has lost a significant fraction of its original thermal energy.

Acknowledgments

PBJ was supported by NASA's GRAIL science team and the Urey Fellows program at the Lunar and Planetary Institute. This paper was improved thanks to reviews by Daniel Moriarty and James Keane. Data associated with this work have been archived with Zenodo using the following DOI: 10.5281/zenodo.2551813

References

Banerdt, W. (1986). Support of long-wavelength loads on Venus and implications for internal structure. *Journal of Geophysical Research: Solid Earth*, *91*(B1), 403–419.

Elkins-Tanton, L. T., Burgess, S., & Yin, Q.-Z. (2011). The lunar magma ocean: Reconciling the solidification process with lunar petrology and geochronology. *Earth and Planetary Science Letters*, *304*(3-4), 326–336.

Evans, A. J., Andrews-Hanna, J. C., Head, J. W., Soderblom, J. M., Solomon, S. C., & Zuber, M. T. (2018). Reexamination of early lunar chronology with GRAIL data: Terranes, basins, and impact fluxes. *Journal of Geophysical Research: Planets*, *0*(0). Retrieved from `https://agupubs.onlinelibrary.wiley.com/doi/abs/10.1029/2017JE005421` doi: 10.1029/2017JE005421

Gagnepain-Beyneix, J., Lognonné, P., Chenet, H., Lombardi, D., & Spohn, T. (2006). A seismic model of the lunar mantle and constraints on temperature and mineralogy. *Physics of the Earth and Planetary Interiors*, *159*(3-4), 140–166.

Garrick-Bethell, I., & Miljković, K. (2018, March). Age of the Lunar South Pole-Aitken Basin. In *Lunar and planetary science conference* (Vol. 49, p. 2633).

Garrick-Bethell, I., & Zuber, M. T. (2009). Elliptical structure of the lunar South Pole-Aitken basin. *Icarus*, *204*(2), 399–408.

Hemingway, D. J., & Matsuyama, I. (2017). Isostatic equilibrium in spherical coordinates and implications for crustal thickness on the Moon, Mars, Enceladus, and elsewhere. *Geophysical Research Letters*.

Herrick, R. R., & Phillips, R. J. (1992). Geological correlations with the interior density structure of Venus. *Journal of Geophysical Research: Planets*, *97*(E10), 16017–16034.

Hiesinger, H., van der Bogert, C. H., Pasckert, J. H., Schmedemann, N., Robinson, M. S., Jolliff, B., & Petro, N. (2012, March). New Crater Size-Frequency Distribution Measurements of the South Pole-Aitken Basin. In *Lunar and planetary science conference* (Vol. 43, p. 2863).

Hirth, G., & Kohlstedt, D. (2013). Rheology of the upper mantle and the mantle wedge: A view from the experimentalists. In *Inside the subduction factory* (p. 83-105). American Geophysical Union (AGU). Retrieved from `https://agupubs.onlinelibrary.wiley.com/doi/abs/10.1029/138GM06` doi: 10.1029/138GM06

Hurwitz, D. M., & Kring, D. A. (2014). Differentiation of the South Pole–Aitken basin impact melt sheet: Implications for lunar exploration. *Journal of Geophysical Research: Planets*, *119*(6), 1110–1133.

James, P. B., Zuber, M. T., & Phillips, R. J. (2013). Crustal thickness and support of topography on Venus. *Journal of Geophysical Research: Planets*, *118*(4), 859–875.

James, P. B., Zuber, M. T., Phillips, R. J., & Solomon, S. C. (2015). Support of long-wavelength topography on Mercury inferred from MESSENGER measurements of gravity and topography. *Journal of Geophysical Research: Planets*, *120*(2), 287–310.

Johnson, B. C., Blair, D. M., Collins, G. S., Melosh, H. J., Freed, A. M., Taylor, G. J., . . . others (2016). Formation of the Orientale lunar multiring basin. *Science*, *354*(6311), 441–444.

Jolliff, B. L., Gillis, J. J., Haskin, L. A., Korotev, R. L., & Wieczorek, M. A. (2000). Major lunar crustal terranes: Surface expressions and crust-mantle origins. *Journal of Geophysical Research: Planets*, *105*(E2), 4197–4216.

Kendall, J. D., & Melosh, H. (2016). Differentiated planetesimal impacts into a terrestrial magma ocean: fate of the iron core. *Earth and Planetary Science Letters*, *448*, 24–33.

Khan, A., Connolly, J., Maclennan, J., & Mosegaard, K. (2007). Joint inversion of seismic and gravity data for lunar composition and thermal state. *Geophysical Journal International*, *168*(1), 243–258.

Konopliv, A. S., Park, R. S., Yuan, D.-N., Asmar, S. W., Watkins, M. M., Williams, J. G., ... others (2014). High-resolution lunar gravity fields from the GRAIL primary and extended missions. *Geophysical Research Letters*, *41*(5), 1452–1458.

Laneuville, M., Taylor, J., & Wieczorek, M. A. (2018). Distribution of radioactive heat sources and thermal history of the moon. *Journal of Geophysical Research: Planets*, *0*(0). Retrieved from `https://agupubs.onlinelibrary.wiley.com/doi/abs/10.1029/2018JE005742` doi: 10.1029/2018JE005742

Laneuville, M., Wieczorek, M., Breuer, D., & Tosi, N. (2013). Asymmetric thermal evolution of the Moon. *Journal of Geophysical Research: Planets*, *118*(7), 1435–1452.

Lemoine, F. G., Goossens, S., Sabaka, T. J., Nicholas, J. B., Mazarico, E., Rowlands, D. D., ... others (2014). GRGM900C: A degree 900 lunar gravity model from GRAIL primary and extended mission data. *Geophysical research letters*, *41*(10), 3382–3389.

Matsuyama, I., Nimmo, F., Keane, J. T., Chan, N. H., Taylor, G. J., Wieczorek, M. A., ... Williams, J. G. (2016). GRAIL, LLR, and LOLA constraints on the interior structure of the Moon. *Geophysical Research Letters*, *43*(16), 8365–8375.

Melosh, H., Freed, A. M., Johnson, B. C., Blair, D. M., Andrews-Hanna, J. C., Neumann, G. A., ... others (2013). The origin of lunar mascon basins. *Science*, *340*(6140), 1552–1555.

Moriarty, D., & Pieters, C. (2016). Impact melt and magmatic processes in central South Pole—Aitken Basin. In *Lunar and planetary science conference* (Vol. 47, p. 1735).

Moriarty, D. P., & Pieters, C. M. (2015). The nature and origin of Mafic Mound in the South Pole-Aitken Basin. *Geophysical Research Letters*, *42*(19), 7907–7915.

Moriarty, D. P., & Pieters, C. M. (2018). The character of South PoleAitken basin: Patterns of surface and subsurface composition. *Journal of Geophysical Research: Planets*, *123*(3), 729-747. Retrieved from `https://agupubs.onlinelibrary.wiley.com/doi/abs/10.1002/2017JE005364` doi: 10.1002/2017JE005364

Neumann, G. A., Zuber, M. T., Wieczorek, M. A., Head, J. W., Baker, D. M., Solomon, S. C., ... others (2015). Lunar impact basins revealed by Gravity Recovery and Interior Laboratory measurements. *Science advances*, *1*(9), e1500852.

Ohtake, M., Uemoto, K., Yokota, Y., Morota, T., Yamamoto, S., Nakamura, R., ... Ishihara, Y. (2014). Geologic structure generated by large-impact basin formation observed at the South Pole-Aitken basin on the Moon. *Geophysical Research Letters*, *41*(8), 2738–2745.

Petro, N. E., & Pieters, C. M. (2004). Surviving the heavy bombardment: Ancient material at the surface of South Pole-Aitken Basin. *Journal of Geophysical Research: Planets*, *109*(E6). Retrieved from `https://agupubs.onlinelibrary.wiley.com/doi/abs/10.1029/2003JE002182` doi: 10.1029/2003JE002182

Pieters, C. M., Head, J. W., Gaddis, L., Jolliff, B., & Duke, M. (2001). Rock types of South Pole-Aitken basin and extent of basaltic volcanism. *Journal of Geophysical Research: Planets*, *106*(E11), 28001-28022. Retrieved from `https://agupubs.onlinelibrary.wiley.com/doi/abs/10.1029/2000JE001414` doi: 10.1029/2000JE001414

Potter, R. W., Collins, G. S., Kiefer, W. S., McGovern, P. J., & Kring, D. A. (2012). Constraining the size of the South Pole-Aitken basin impact. *Icarus*, *220*(2), 730–743.

Roberts, J. H., & Zhong, S. (2006). Degree-1 convection in the martian mantle and the origin of the hemispheric dichotomy. *Journal of Geophysical Research: Planets*, *111*(E6).

Shoemaker, E., Robinson, M., & Eliason, E. (1994). The south pole region of the Moon as seen by Clementine. *Science*, *266*(5192), 1851–1854.

Smith, D. E., Zuber, M. T., Neumann, G. A., Lemoine, F. G., Mazarico, E., Torrence, M. H., ... others (2010). Initial observations from the lunar orbiter laser altimeter (LOLA). *Geophysical Research Letters*, *37*(18).

Sori, M. M., James, P. B., Johnson, B. C., Soderblom, J. M., Solomon, S. C., Wieczorek, M. A., & Zuber, M. T. (2018). Isostatic compensation of the lunar highlands. *Journal of Geophysical Research: Planets*, *123*(2), 646–665.

Speyerer, E., Robinson, M., Denevi, B., et al. (2011). Lunar reconnaissance orbiter camera global morphological map of the moon. In *Lunar and planetary science* *conference* (Vol. 42, p. 2387).

Uemoto, K., Ohtake, M., Haruyama, J., Matsunaga, T., Yamamoto, S., Nakamura, R., . . . Iwata, T. (2017). Evidence of impact melt sheet differentiation of the lunar South Pole-Aitken basin. *Journal of Geophysical Research: Planets*.

Vaughan, W. M., & Head, J. W. (2014). Impact melt differentiation in the South Pole-Aitken basin: Some observations and speculations. *Planetary and Space Science*, *91*, 101–106.

Wieczorek, M. A., Neumann, G. A., Nimmo, F., Kiefer, W. S., Taylor, G. J., Melosh, H. J., . . . others (2013). The crust of the Moon as seen by GRAIL. *Science*, 1231530.

Wieczorek, M. A., & Phillips, R. J. (1998). Potential anomalies on a sphere: Applications to the thickness of the lunar crust. *Journal of Geophysical Research: Planets*, *103*(E1), 1715–1724.

Wilhelms, D. E., John, F., & Trask, N. J. (1987). *The geologic history of the Moon* (Tech. Rep.).

Zuber, M. T., Smith, D. E., Lehman, D. H., Hoffman, T. L., Asmar, S. W., & Watkins, M. M. (2013). Gravity Recovery and Interior Laboratory (GRAIL): Mapping the lunar interior from crust to core. *Space Science Reviews*, *178*(1), 3–24.

Zuber, M. T., Smith, D. E., Watkins, M. M., Asmar, S. W., Konopliv, A. S., Lemoine, F. G., . . . others (2013). Gravity field of the Moon from the Gravity Recovery and Interior Laboratory (GRAIL) mission. *Science*, *339*(6120), 668–671.

Figure 1.

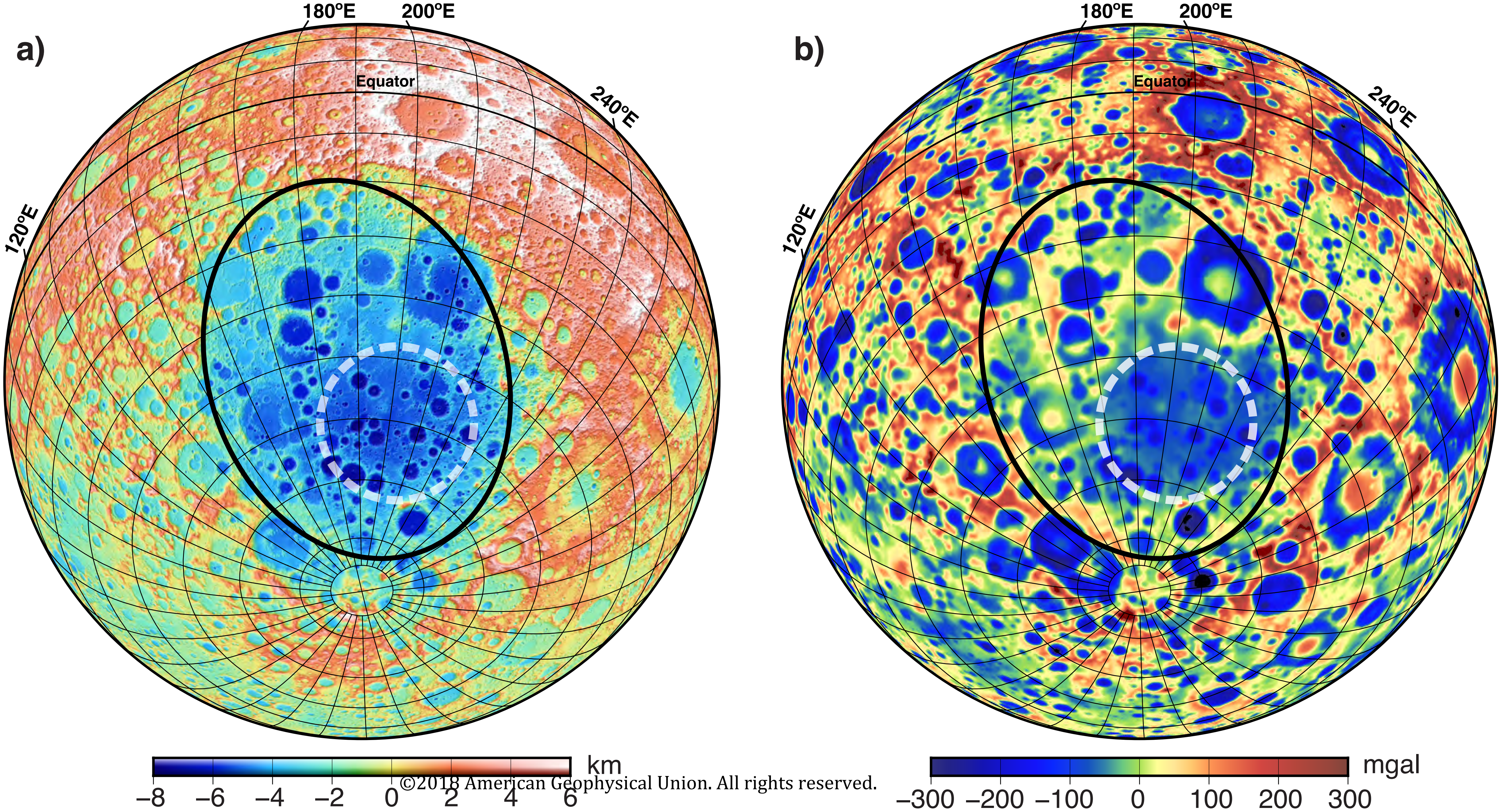
a)
b)
180°E
200°E
240°E
120°E
Equator
km
−8
−6
−4
−2
0
2
4
6
mgal
−300
−200
−100
0
100
200
300

Figure 2.

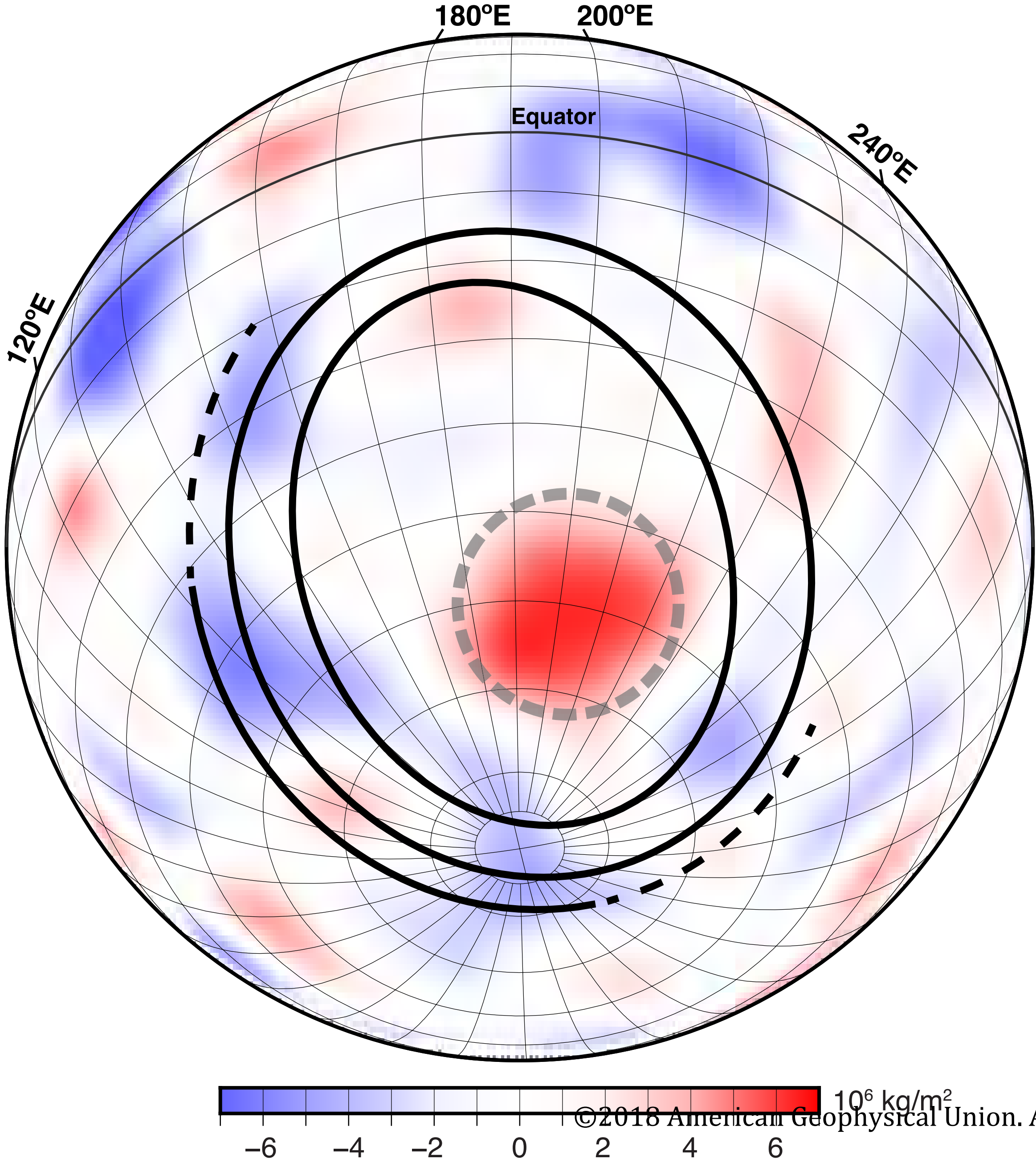
180°E
200°E
240°E
120°E
Equator
10^6 kg/m^2
−6
−4
−2
0
2
4
6

Figure 3.

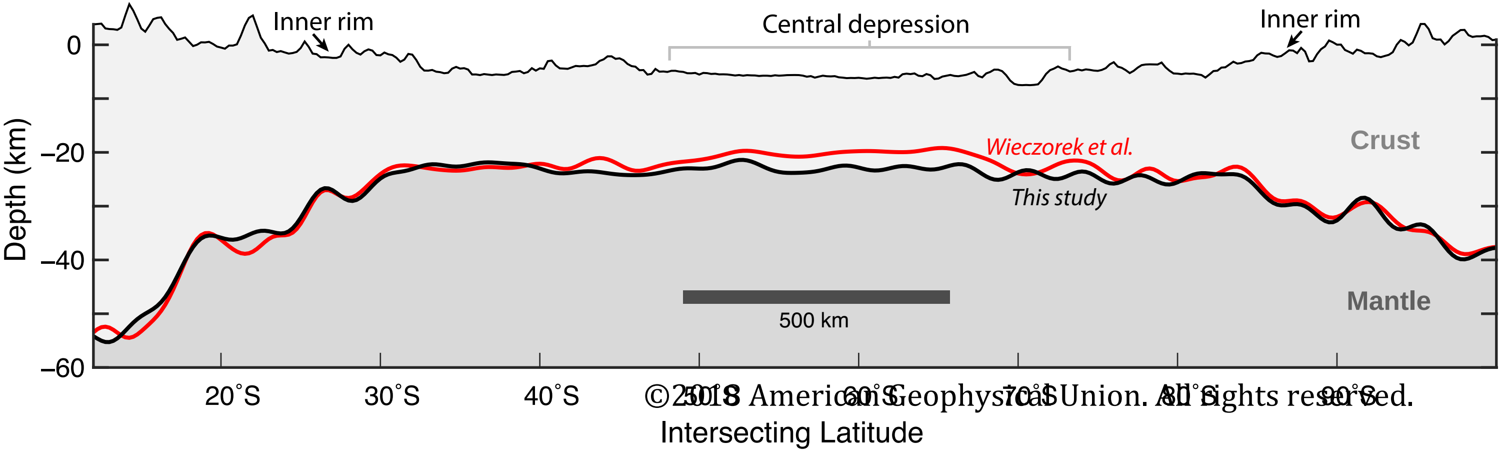

Inner rim
Central depression
Inner rim
0
−20
−40
−60
Depth (km)
Crust
Wieczorek et al.
This study
Mantle
500 km
20˚S
30˚S
40˚S
50˚S
60˚S
70˚S
80˚S
90˚S
Intersecting Latitude

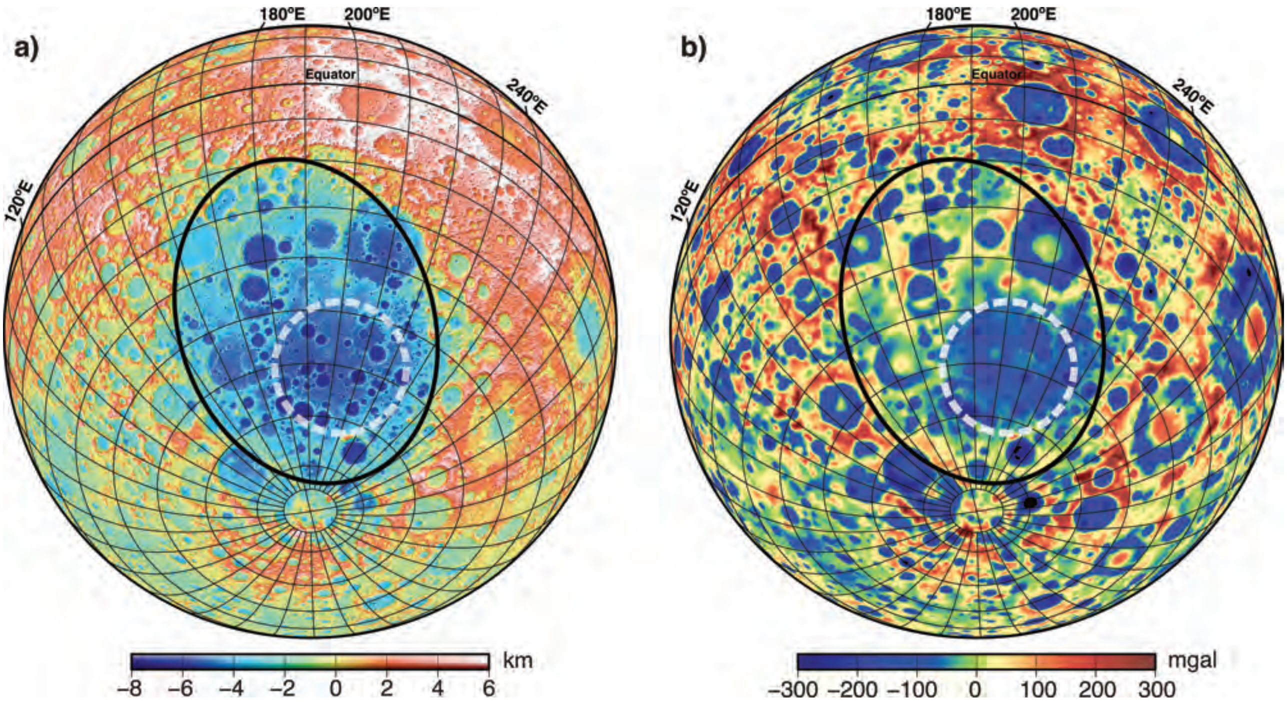

2019gl082252-f01-z-.eps

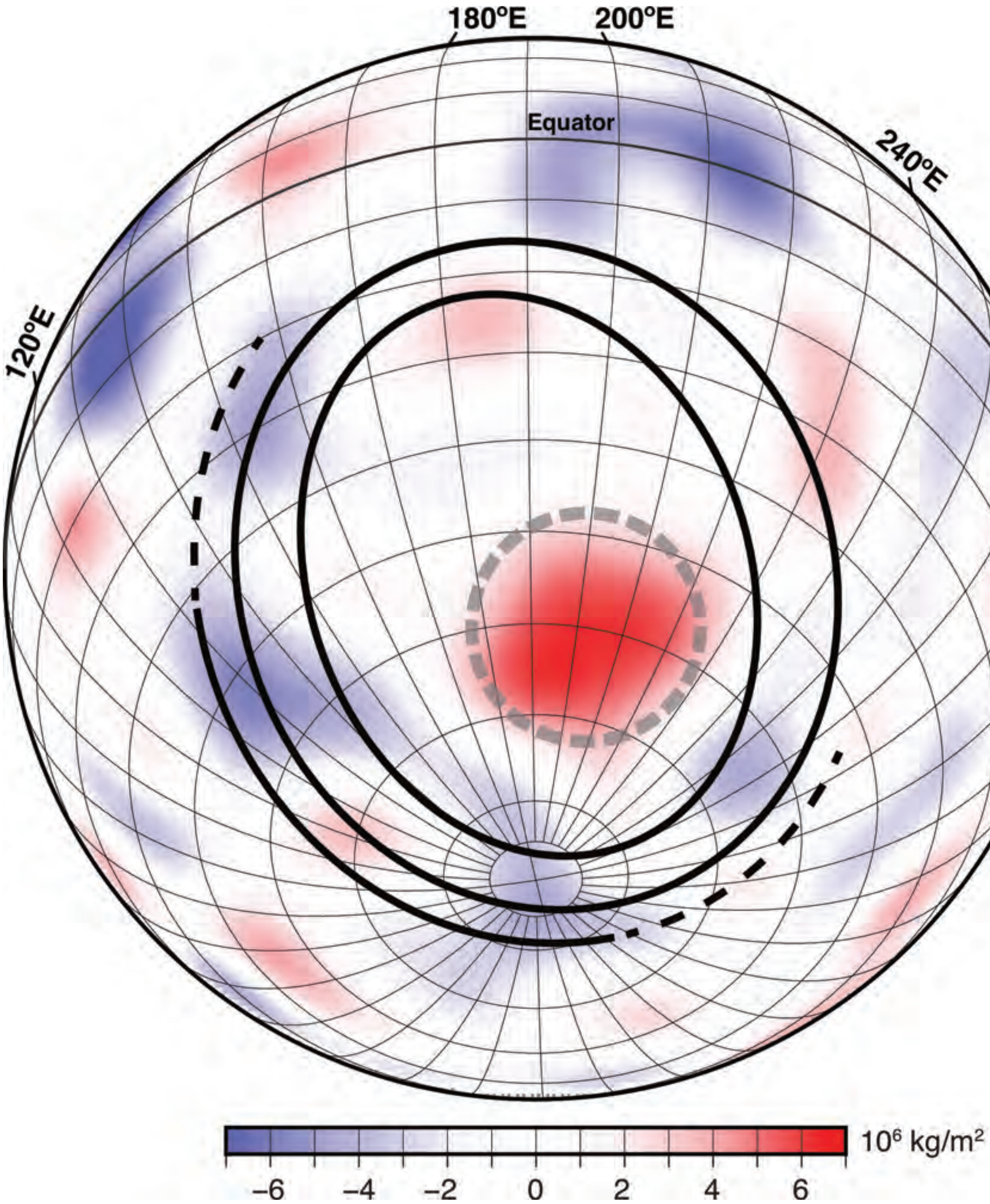

2019gl082252-f02-z-.eps

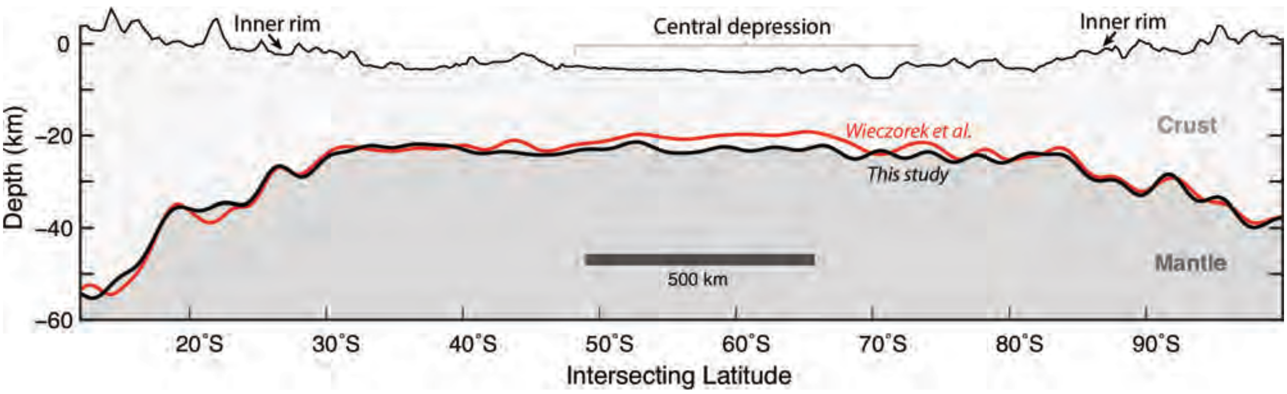

2019gl082252-f03-z-.eps